PNAS RESEARCH ARTICLE | BIOPHYSICS AND COMPUTATIONAL BIOLOGY

Toward understanding lipid reorganization in RNA lipid nanoparticles in acidic environments

Adiran Garaizar[a,b], David Díaz-Oviedo[a], Nina Zablowsky[c], Sami Rissanen[d], Johannes Köbberling[a], Jiawei Sun[e], Christoph Steiger[e], Patrick Steigemann[c], Florian A. Mann[e,1], and Katharina Meier[a,1]

Affiliations are included on p. 8.

Edited by Catherine Murphy, University of Illinois at Urbana-Champaign, Urbana, IL; received March 5, 2024; accepted October 2, 2024

The use of lipid nanoparticles (LNPs) for therapeutic RNA delivery has gained significant interest, particularly highlighted by recent milestones such as the approval of Onpattro and two mRNA-based SARS-CoV-2 vaccines. However, despite substantial advancements in this field, our understanding of the structure and internal organization of RNA-LNPs –and their relationship to efficacy, both in vitro and in vivo– remains limited. In this study, we present a coarse-grained molecular dynamics (MD) approach that allows for the simulations of full-size LNPs. By analyzing MD-derived structural characteristics in conjunction with cellular experiments, we investigate the effect of critical parameters, such as pH and composition, on LNP structure and potency. Additionally, we examine the mobility and chemical environment within LNPs at a molecular level. Our findings highlight the significant impact that LNP composition and internal molecular mobility can have on key stages of LNP-based intracellular RNA delivery.

lipid nanoparticles | RNA delivery | mRNA therapeutics | MD simulations | endosomal escape

Nucleic acid-based therapies have emerged as promising alternatives for developing potential treatments for a wide range of disorders previously considered undruggable. The field of mRNA therapeutics, where mRNA is used to induce protein expression, has gained significant attention in recent years driven by the development and approval of mRNA-based vaccines during the COVID-19 pandemic. Currently, several potential mRNA-based therapies are being evaluated in clinical trials in the fields of oncology, vaccines, immunology, protein replacement therapies, and genome editing (1). However, due to its intrinsic instability and large size, mRNA should be encapsulated in a delivery vehicle to protect it from degradation en route to the target cell as well as to enable uptake into the cytosol (2). To this end, lipid nanoparticles (LNPs) are by far the most advanced nonviral RNA delivery system (2, 3), as evidenced by the approval of several RNA-LNP-based drugs in recent years. Notable examples include Patisiran (Onpattro®), an LNP-based siRNA therapy for treating polyneuropathies resulting from hereditary transthyretin amyloidosis (hATTR), as well as the mRNA-based vaccines against COVID-19 from Pfizer-BioNTech (BNT162b2) (4) and Moderna (mRNA-1273) (5). Given the significant potential and rapid development of this lipid-based vector, the current status and challenges of LNPs have been extensively reviewed in recent years (1, 2, 6, 7).

LNPs typically range from 50 to 120 nm in size and generally consist of four lipid components: a (cationic) ionizable lipid (CIL), cholesterol, a phospholipid, and a poly(ethylene glycol) (PEG)-derived lipid. Several properties, such as LNP size and the nature of the ionizable lipid, have been shown to influence LNP performance both in vitro and in vivo (8–10). However, the distribution of components within the particle and the presence of nanostructured regions remain subjects of active research. Early molecular dynamics (MD) simulations and experiments suggested an inverse micellar arrangement of the ionizable lipids encapsulating siRNA (10–12). Subsequent studies on mRNA-LNPs, including those from Yanez-Arteta et al. (8) and Sebastiani et al. (13), propose the existence of inverse worm-like micellar phases. For siRNA-LNPs, Kulkarni et al. (14, 15) postulate a lamellar structure primarily consisting of DSPC–cholesterol concentric bilayers with siRNA sandwiched in between. In contrast, Cornebise et al. (9) observed both amorphous and multilamellar-core structures for mRNA-LNPs. Overall, the structure of mRNA-LNPs appears to be largely dependent on the nature of the ionizable lipid (16), the cargo, as well as different formulation parameters such as the N:P ratio and pH (17, 18). Additionally, recent reports from Trollmann et al. (19) and Paloncýová et al. (20) regarding atomistic MD simulations of size-reduced LNP systems (20 to 35 nm diameter) support the presence of an inverse worm-like micellar structure, consistent with findings from recent experimental studies (8, 13, 21). However, despite the great contributions from these studies,

Significance

Our research offers insights into the design of lipid nanoparticles (LNPs), an advanced delivery system for RNA-based therapies, including some of the mRNA vaccines developed during the COVID-19 pandemic. Through advanced molecular simulations, we investigated how variations in LNP composition influence their structural dynamics and RNA release within cells. These dynamic structural changes can be crucial for enhancing RNA delivery efficiency. Our findings contribute to the development of effective tools for rapid screening of LNPs, by reducing the variable space for formulation optimization, which could, in turn, accelerate the advancement of RNA therapeutics. This work not only enhances our understanding of LNPs but also underscores the potential of computational methods to support innovative drug formulation.

Author contributions: A.G., F.A.M., and K.M. designed research; A.G., N.Z., P.S., and F.A.M. performed research; A.G., N.Z., S.R., J.K., J.S., C.S., and P.S. contributed new reagents/analytic tools; A.G., D.D.-O., N.Z., P.S., F.A.M., and K.M. analyzed data; and A.G., D.D.-O., and F.A.M. wrote the paper.

Competing interest statement: All authors are current employees of Bayer AG or Nuvisan ICB GmbH.

This article is a PNAS Direct Submission.

[1] To whom correspondence may be addressed. Email: florian.mann@bayer.com or katharina.meier2@bayer.com

This article contains supporting information online at https://www.pnas.org/lookup/suppl/doi:10.1073/pnas.2404555121/-/DCSupplemental.

further understanding of the influence of composition and size on the internal architecture of full-sized LNPs is needed, with a special focus on the LNP structure in the maturing endosome, since this is where the process of endosomal escape takes place, which is known to be a crucial bottleneck in functional RNA delivery (22, 23). Before cellular uptake, LNPs are thought to undergo a process called "PEG-shedding" (24–26), in which PEGylated lipids located at the surface (10, 11, 27) desorb from the LNP in exchange for serum proteins such as apolipoprotein E (ApoE). This process has been shown to be pivotal for LNP potency and liver tropism in vivo (28). Recent studies indicate that after endocytosis, the protein corona detaches from the nanoparticles, facilitating endosomal escape (29, 30).

In this work, we simulated full-size LNPs in environments with varying degrees of acidification to better understand the state of LNPs in an endosome-like microenvironment. Gaining improved insight into the structural and dynamic characteristics of LNPs under these specific conditions presents a significant opportunity for the rational design and optimization of next-generation LNPs. Additionally, to further explore how these factors might modulate LNP activity, we conducted cell assays on those simulated formulations, providing insight into LNP performance at various stages of intracellular delivery.

Results and Discussion

Direct Coexistence Enables Simulations of Full-Size LNPs. At the onset of our study, we conducted direct coexistence simulations (DC) (31–33) to investigate how LP01 (34), a CIL currently used in a clinical-stage gene editing study (35), along with cholesterol, distearoylphosphatidylcholine (DSPC), and RNA, arranges within an LNP in an acidic environment. To ensure the accuracy of our model, we evaluated the influence of pegylated lipids on LNP structure. These simulations revealed that PEG-lipids, whether partially or fully retained, remain localized on the LNP surface without significantly disrupting the overall lipid organization, (*SI Appendix*, Fig. S7). In light of these results, and considering the prolonged equilibration times inherent to polymer simulation that scale quadratically with the number of repeating units (36), we excluded PEG-lipids from our primary model. This allowed us to focus on the core components of the LNP –cationic ionizable lipid, cholesterol, DSPC, and RNA– thereby enhancing the throughput of this approach.

Direct coexistence (DC) enables the simulation of multiple full-sized LNPs within a realistic timeframe by placing a rectangular segment of the nanoparticle in coexistence with the external aqueous medium, as depicted in Fig. 1. To model the LNP components, we employed coarse-grained (CG) molecular dynamics (MD), an expanding area of research that has gained traction due to seminal works reformulating coarse-graining as a machine-learning problem (37–39). Due to its transferability (40–44) and extensive validation (45), we used the MARTINI 3 model (45) (nontitratable version (46, 47); further details can be found in the *SI Appendix*, *Methods*). Direct coexistence can also be used with atomistic models, allowing for studies with greater detail of interactions (48).

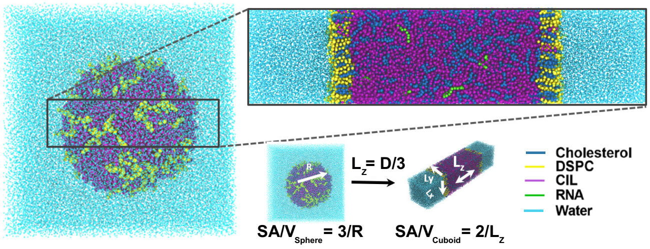

Fig. 1. Coarse-grained molecular dynamics (MD) simulations: setup. In a direct coexistence (DC) simulation, a rectangular segment of the nanoparticle is set in coexistence with the external aqueous medium (top right). The rectangular segment length (Lz) is chosen to ensure that its Surface-Area-to-Volume ratio (SA/V =2/Lz) is equivalent to that of the LNP (SA/V =3/R), where R is the radius of the LNP and D its diameter.

For this study, we selected two LNPs with significantly different lipid compositions: *LNP1* (LP01/cholesterol/DSPC = 45:45:10, molar ratios) and *LNP2* (73:18:9), while maintaining a constant N/P ratio (molar proportion between CIL-amine and RNA-phosphate groups) of 4.5 in both cases. Experimentally, these formulations resulted in LNPs with DLS-measured diameters of 99 nm and 198 nm, respectively (*SI Appendix*, Table S1). Compositions highly enriched in ionizable lipid have previously been studied in the context of siRNA-LNPs (15) and ASO-LNPs (49), and were associated with lower nucleic acid encapsulation and the formation of "bleb" structures, making them interesting targets for our MD-guided structural evaluations.

During the setup of the simulations, the size of the DC simulation boxes (Fig. 1) was chosen to ensure equivalence with the experimentally measured radii by matching the Surface Area-to-Volume (SA/V) ratio. This parameter modulates the distribution of components at the surface versus in the interior of the LNP.

Simulating LNPs at a reduced size results in artificially high surface area-to-volume (SA/V) ratios and corresponding overenrichment of the surface (8, 50), as well as inaccurate Laplace pressure (51). Moreover, given the typical molecular size (Rg) of approximately 0.4 nm inside LNPs, the local surface curvature can be considered negligible for particles with a radius greater than 35 nm. In this context, direct coexistence (DC) offers an alternative simulation approach to accurately study component distribution along the LNP at a significantly reduced computational cost compared to direct simulations of full-sized LNPs. Indeed, DC simulations of *LNP1* consisted of ~50.000 particles, while direct simulations of a 100 nm LNP would require around 21 million particles, and up to 170 million for a 200 nm LNP [extrapolated from about 7.2 million for a 70 nm LNP (19)].

While *LNP1* (diameter = 99 nm) falls within the size range commonly observed for RNA-LNPs, the CIL-enriched formulation *LNP2* is substantially larger (198 nm diameter), a phenomenon previously attributed to the electrostatic repulsion of excess ionizable lipid (49). Additionally, a high concentration of lipid could increase the interfacial free energy with water, leading to larger average sizes for the LNPs.

LNP Composition can Markedly Alter the Core-Shell Architecture. For both simulated formulations, we computed the average concentration profile of each molecular species, as well as the total charge density profile at different distances from the center of the LNP (Fig. 2 *A* and *C*). Due to the difference in topology (spherical vs rectangular), the distances are contracted (e.g., a diameter of 100 nm is equivalent to a 33 nm-long box).

Our simulations indicated the presence of a core-shell architecture, with an outer shell characterized by a high content of DSPC, similar to previous studies of LNPs under neutral conditions (8, 13, 19, 20). This aligns with recent reports from small angle neutron scattering (SANS) experiments for MC3-LNPs in the Onpattro formulation (8 13), which provided insights into the distribution of lipid components between the core and shell (*shell:* 51% cholesterol, 28% MC3, 18% DSPC, and 2.7% DMPE-PEG; *core:* 24% cholesterol, 76% MC3, and 0.033% mRNA) (13). However, using these values for comparative purposes should be approached with caution, as they correspond to LNPs of different sizes and under neutral conditions (such as during storage or in the bloodstream), which typically involve a lower concentration

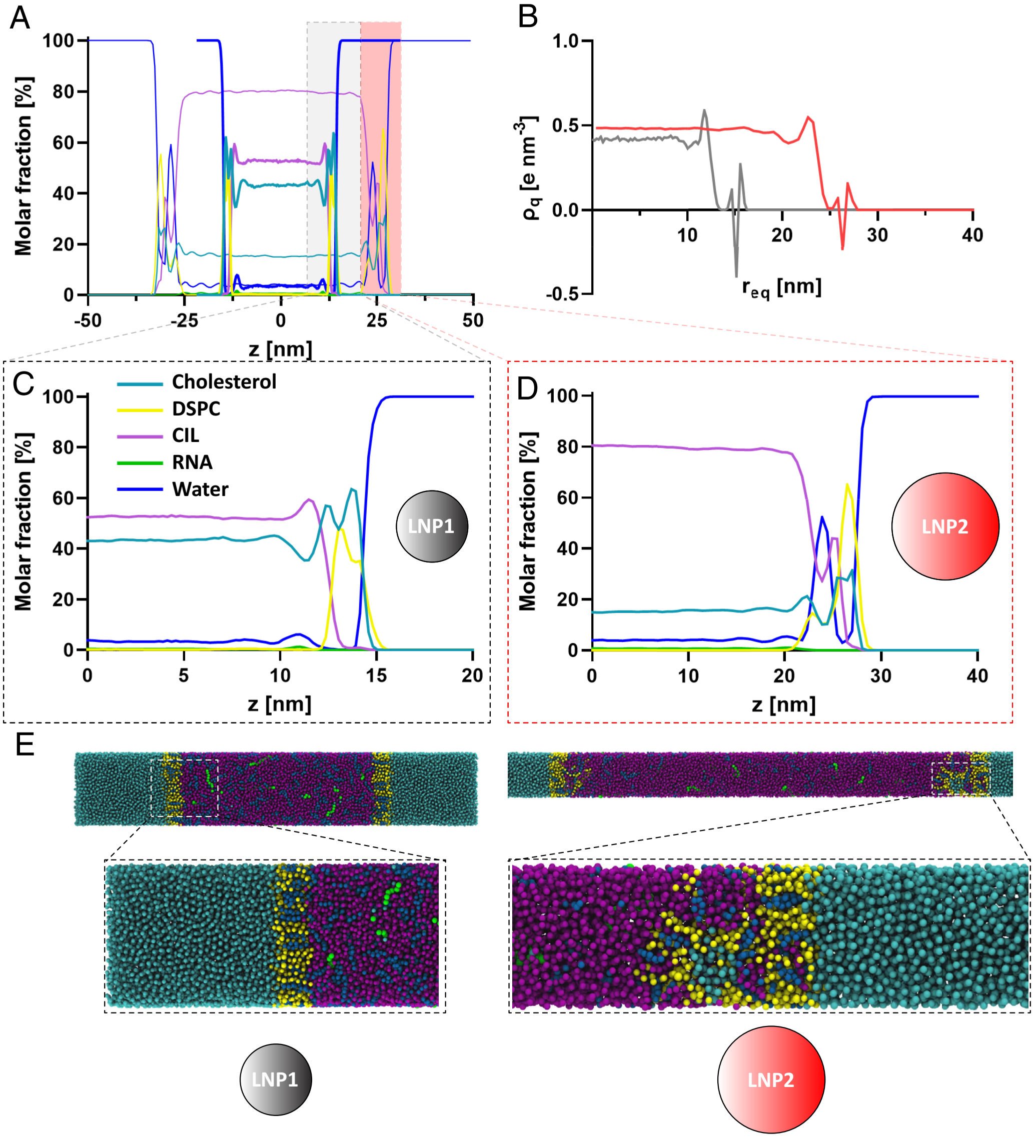

Fig. 2. Concentration and charge density profiles for *LNP1* and *LNP2*. (*A*) Molar concentration profiles as a function of the distance to the LNP center for *LNP1* (thick lines) and *LNP2* (thin lines); (*B*) charge density profile as a function of the distance to the LNP center for both *LNP1* and *LNP2*; (*C* and *D*) concentration profiles for *LNP1* and *LNP2*, respectively (1 nm in a spherical LNP is equivalent to 0.33 nm in a DC simulation); (*E*) close-up snapshot of the core-shell-water interphases for the studied LNPs.

of protonated amines. Comparison between our studied formulations (*LNP1* and *LNP2*) in an environment where most of the CIL molecules are charged revealed significant differences in the compositions of the outer shells, as depicted in Fig. 2.

We defined the outer shell as the region where concentration profiles significantly differ from the bulk values. For *LNP1*, this corresponds to the region at ~10 to 15 nm on the *x*-axis (Fig. 2*C*). However, a more complex scenario was observed for *LNP2* (Fig. 2*D*). First, analogous to *LNP1*, we identified a primary shell region (~21 to 27 nm on the *x*-axis, further referred to as the "micellar" region) with molecules up to 6.5 nm away from the bulk. Additionally, a second, DSPC-rich outer shell was detected up to 3 nm beyond the micellar region (27 to 30 nm on the *x*-axis). For the outermost, solvent-exposed shells, we found the following molar compositions: for *LNP1*, 47.0% cholesterol, 38.2% CIL, 14.5% DSPC, and 0.3% RNA; for *LNP2*, 27.0% cholesterol, 6.5% CIL, 66.2% DSPC, and 0.3% RNA. The "micellar" region of *LNP2* is composed of 24.2% cholesterol, 48.6% CIL, 26.5% DSPC, and 0.7% RNA. A closer examination of the outermost shells (in contact with water) reveals that the zwitterionic heads of DSPC molecules are located at the LNP surface, exposed to the solvent, while the aliphatic tails remain buried in the lipophilic environment of the nanoparticle. In the case of *LNP1* (formulation with 45% CIL, Fig. 2*A*), an overenrichment of cholesterol molecules in the shell compared to the core is observed, likely due to favorable DSPC–cholesterol interactions (15) and the limited solubility of cholesterol in the CIL-rich core (8, 14). Similarly, the protonated CIL-amine moiety contributes to the presence of this substance in the surface monolayer. In contrast, the CIL-enriched formulation *LNP2* displays a higher concentration of CIL at the surface, resulting in a reduced cholesterol concentration. Moreover, we observed DSPC–water micelle-like structures (Fig. 2*E* – inset), which may arise from the LNP surface being saturated with DSPC molecules due to the smaller available surface area (1.27 DSPC molecules per nm^2 for *LNP1* vs 2.2 DSPC molecules per nm^2 for *LNP2*).

The reduced available space at the surface likely promotes a higher concentration of DSPC in the interior of the LNP, which subsequently rearranges to form water-containing micelles that may dissolve, merge, or diffuse over longer timescales. Such micellar, or even "bleb," structures at the LNP surface align with previous experimental observations (52) and are associated with high local concentrations of ionizable lipid (49). We hypothesize that these micellar nanostructures could interfere with LNP-membrane or LNP-serum protein interactions, ultimately hindering subsequent uptake and endosomal escape processes. This interference may occur through steric hindrance of functional RNA release or competitive fusion of the water-containing micelles with the endosomal membrane. It is important to note that changes in lipid content and morphology of both the surface and core are likely critical determinants of endosomal escape. This is supported by recent reports from Patel et al. (53) and Zheng et al. (54) which demonstrated that cubic and inverse hexagonal phases lead to faster fusion with endosomal membranes.

Charge Distributions are Similar for Both Lipid Compositions. Another important parameter for LNP characterization is the surface charge, as it can play a key role in LNP performance in vivo, depending on the nanoparticle composition. As mentioned earlier, the charged molecules at the shell are exposed to serum proteins, which can alter the biodistribution of RNA-LNPs, potentially enabling engineered particles to target specific organs or cells of interest (14). In this context, molecular dynamics (MD) can be applied to prioritize formulations based on their expected surface charges. After obtaining profiles for the total charge density at different distances from the LNP center (Fig. 2*B*), we observed that both studied formulations exhibit similar charge profiles. In the core, the charges are homogeneously distributed, although *LNP1* shows a slightly lower charge density, likely due to its lower content of CIL. At the surface, both formulations display an alternating charge density, attributable to the zwitterionic nature of regularly arranged DSPC molecules, followed by a positive charge peak, which can be attributed to the presence of protonated CIL-amines on the surface and their favorable interactions with the solvent.

Linking Structure and Activity using Cell Assays. Motivated by the previous findings from MD simulations, we next tested two different RNA-LNP formulations on cells. For this, we applied a fluorescence microscopy-based assay, recently developed by Munson et al. (55), which can visualize and quantify crucial steps in LNP delivery (22, 23, 55): uptake, endosomal escape, and RNA translation. HepG2 and HeLa cells, stably expressing an N-terminally fluorescently labeled Galectin-9 (Gal9) protein, were treated with green fluorescent protein (GFP)-encoding mRNA-LNPs, and monitored by time-lapse imaging for 24 h.

RNA uptake was evaluated by measuring Cyanine-5 (Cy5)-labeled mRNA; endosomal escape was analyzed by counting Gal9 spots per cell region; and translation efficacy was assessed by monitoring the fluorescence intensity of expressed GFP. In general, *LNP1* displayed more efficient uptake and endosomal escape, as well as a higher GFP expression when compared to *LNP2* in both cell lines (Fig. 3*C*). It is important to note that this assay cannot differentiate between endosomal escape from early or late endosomes. Studies by Paramasivam et al. (29), Zheng et al. (54), and Wittrup et al. (56) have shown that there is a narrow time window for functional release from endosomes. By correlating the results from these cell assays with those from the MD simulations described above, we can hypothesize that surface composition and organization (including the presence of nanostructures, such as micellar regions) are important factors for LNP activity in cells. Further research is needed to precisely determine how much of the variance observed in LNP performance across formulations or CIL modifications is explained by structurally derived variables.

Ideally, such a combination of in vitro experiments and structural simulations could be developed into a high-throughput tool to enhance our understanding of LNP structure–activity relationships (SARs). These SARs can pave the way to link the molecular structure of formulation components to LNP activity, ultimately leading to the development of more potent LNP formulations.

The Interior of LNPs Is not Homogeneous but Consists of Transient Nanostructures. Given the strong in vitro performance exhibited by *LNP1*, we focused on this formulation as an illustrative example to gain deeper insights into the chemical environment surrounding water and RNA molecules inside of an LNP through simulations. To avoid pollution from the water-lipid interphase, we conducted simulations of the core region of LNPs, specifically bulk NpT simulations at T = 298 K and P = 1 bar. The composition of the LNP core (*SI Appendix*, Supporting Information) was derived from the DC simulations by averaging the composition from 0 to 10 nm from the center of the LNP in Fig. 2*C*.

This more detailed analysis revealed that the components are not homogeneously distributed; rather, they form different nanostructures, similar to previous experimental reports (8, 13, 21). These nanostructures, usually in the shape of inverse (worm-like) micelles (Fig. 4 *B* and *C*), are transient and do not coalesce; instead, they dissolve and reform in different locations within the LNP over time. This dynamic nature leads to the previously presented density profiles (Fig. 2 *A* and *C*), which show a homogeneous component distribution inside the LNPs, even though the overall structure at a given time is predominantly (inverse) micellar.

The radial distribution functions ($g(r)$) for each component, relative to either water or RNA, were computed to provide a quantitative assessment of their coordination and chemical environment, as illustrated in Fig. 4 *D* and *E*, respectively. These functions indicate the enrichment or depletion of specific components at a given distance from water or RNA molecules compared to the average concentration inside the LNP.

Fig. 4*D* shows high peaks for the water–water function at short distances, suggesting the presence of small water clusters in an environment with low bulk water content, such as the interior of these inverse micelles in LNPs. The water–RNA and water–DSPC functions indicate that the internal water droplets are enriched in RNA and DSPC, consistent with the existence of inverse micellar structures within the LNPs. This aligns with previous reports (8, 13) indicating that the environment surrounding RNA in LNPs is predominantly aqueous (8). The water $g(r)$ functions for both CIL and cholesterol exhibit significantly lower peaks, indicating higher concentrations of these two lipids in the bulk phase.

Similarly, we computed the radial distribution functions of RNA relative to other molecular species within the LNP to understand their spatial arrangement around RNA. Consistent with the proposed reverse micelle nanostructures, where RNA is organized within the LNP interior (as depicted in Fig. 4 *A* and *C*), we find that the first solvation shell of RNA is highly enriched in CIL and water (Fig. 4*E*). CIL molecules are preferentially distributed around RNA at their bonding distance, as expected given their role in sequestering RNA into LNPs by binding to the RNA phosphate backbone with their charged amine moieties. The radial distribution functions for both DSPC and cholesterol indicate a depletion of these components, likely due to steric exclusion by the ionizable lipid and water molecules surrounding the RNA. The RNA–RNA distribution reveals a depletion region up to approximately 3 to 6 nm, which can be explained by the center-to-center distances of approximately 6 nm between RNA-containing channels or inverse worm-like micelles formed by the CIL molecules. This observation is also consistent with published SAXS data on LNPs containing other ionizable lipids (8).

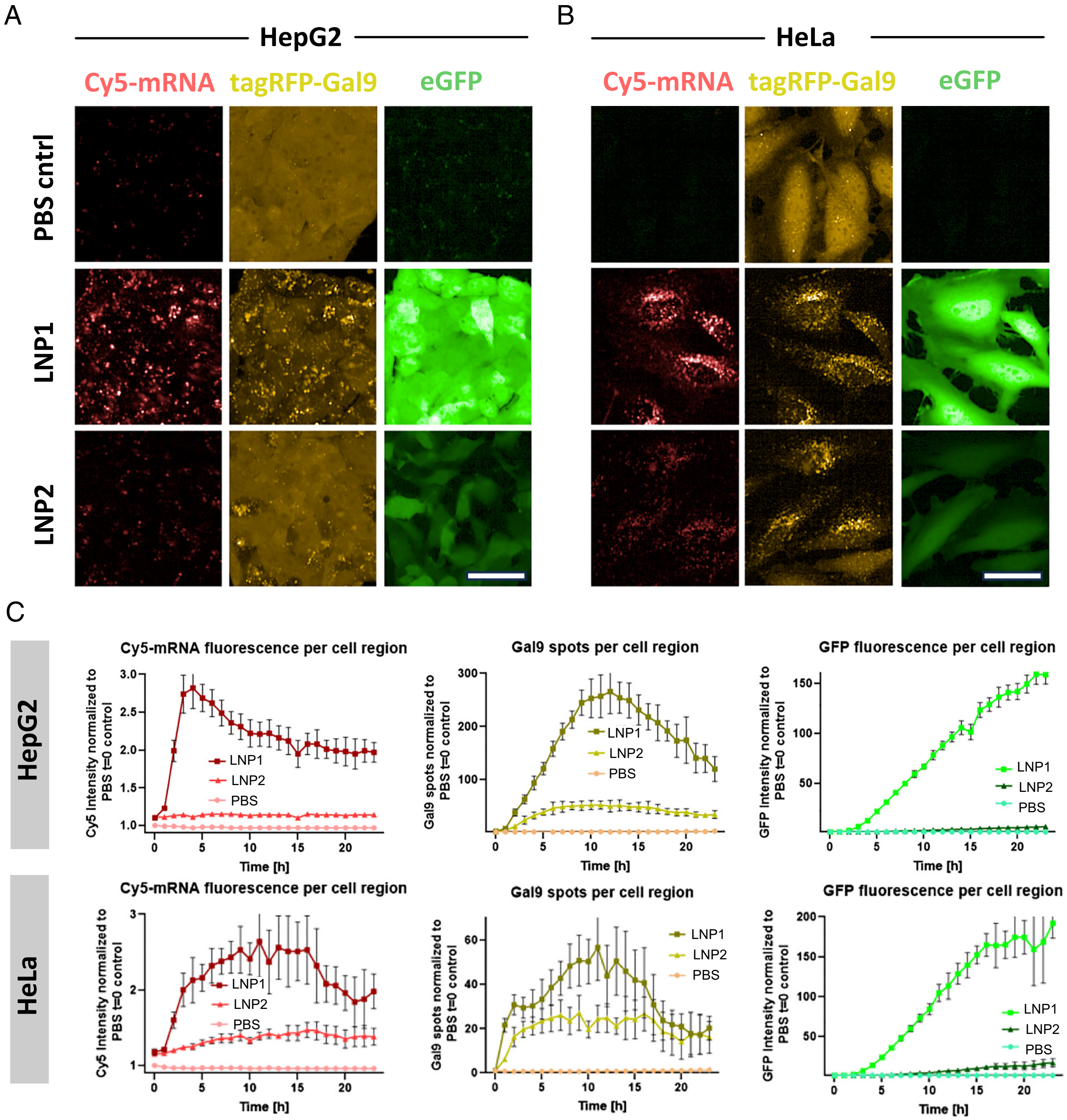

Fig. 3. Deciphering the relationship between the (modeled) LNP structures and their function on different cells. (*A*) HepG2 and (*B*) HeLa cells constitutively expressing fluorescently labeled Gal9 were treated with 1 μg/mL LNP containing Cy5-labeled, GFP-encoding mRNA and followed by live-cell imaging (1 picture per hour) for 24 h; (*C*) mRNA entry and translation was measured by quantification of Cy5 or GFP response in the region of the cells, and endosomal escape was assessed by quantification of Gal9 spots per region of cells. All data were normalized to $t = 0$ of the negative control (PBS) in the respective readout. Error bars = SD. Exemplary data from two independent experiments with similar outcome. (Scale bar (parts *A* and *B*), ~40 μm.)

DSPC Precludes RNA Efflux Under Environmental pH Variations. We recognized the potential of our simulations to better understand the pH-dependent behavior of LNPs, given the critical importance of this parameter both in the LNP manufacturing process and during cargo release through endosomal escape. First, we simulated an increase in pH until no further CIL-amine groups were protonated, resembling the neutralization step following particle formation in the LNP manufacturing process (Fig. 5 *A* and *B*). In agreement with experimental observations, but contrary to recent simulation-based reports (20), our results showed that RNA remained encapsulated even after neutralizing all CIL-derived positive charges in the interior of the LNP. Next, inspired by a recently described method of RNA entrapment into preformed empty LNPs (57, 58), and the high potential of this approach for rapid screening of different mRNA (or sgRNA) formats, we simulated a preformed LNP and subsequently added RNA to the aqueous phase. As expected, RNA quickly penetrated the LNP when the amine groups were protonated, whereas it remained on the LNP surface under neutral conditions (see Supporting Information for simulation movies).

In contrast to other recent MD simulations (19, 20), our results suggest that, despite the affinity of encapsulated RNA for the aqueous phase at neutral pH, it cannot migrate out of the LNP. However, removal of the DSPC outer layer from this system at neutral pH resulted in RNA migrating to the aqueous phase (Fig. 5*C*). Therefore, we postulate that the DSPC layer at the surface acts as

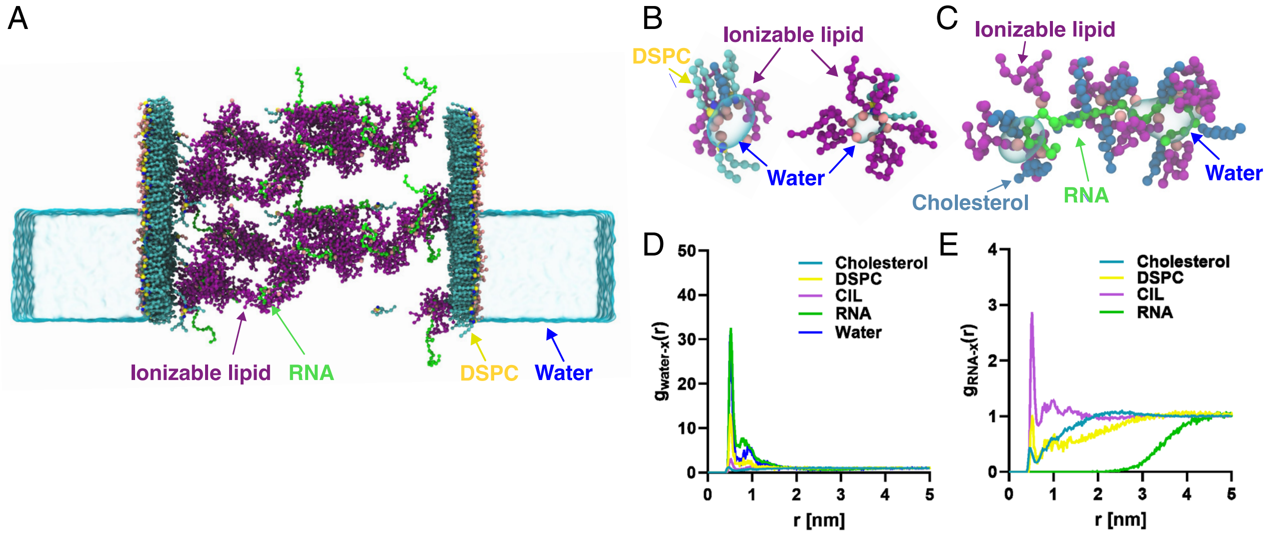

Fig. 4. Characterization of the internal nanostructures and chemical environment around RNA and water within LNPs. (*A*) Visualization of the reverse micellar LNP interior from a direct coexistence simulation (one extra periodic neighbor is included, perpendicular to the interface). The render highlights exterior water, DSPC (cyan tails) to visually reference the LNP surface, RNA (green), and its bound CIL (purple), whereas other components have been rendered transparent to enhance clarity; (*B*) snapshots of reverse water micelles (left: DSPC-rich; right: CIL-rich) taken from a simulation of the interior of an LNP; (*C*) snapshot of a reverse micelle around RNA taken from a simulation of the interior of an LNP; (*D*) radial distribution function of water molecules to LNP-components; (*E*) radial distribution function of RNA molecules to LNP-components. In the snapshots, only molecules in contact—within one bead's diameter—with the water cluster or RNA molecule, respectively, are shown. The surface of water molecules has been rendered transparent for visualization.

a valve, allowing RNA entry at low pH while preventing its release at higher pH values, in agreement with previous experimental observations by Kulkarni et al. (15) Interestingly, we noted a shift of CIL molecules toward the LNP surface at lower pH (*SI Appendix*, Fig. S6). This supports the hypothesis of an endosomal escape process based on membrane fusion events and mediated by charged ionizable lipid headgroups (10), rather than by LNP breakage inside the endosome (29) and the escape of smaller RNA–CIL complexes. Our simulations showing the CIL relocating toward the surface align with the cargo release mechanism proposed earlier by Maugeri et al. (59), where CIL molecules previously not bound to RNA ("excess CIL") induce membrane fusion and disruption, followed by the escape of the RNA–CIL "complex salt" (1:1 molar ratio RNA nucleotide to ionizable lipid amine) into the cytosol. As illustrated in *SI Appendix*, Fig. S7, the retention of PEG-lipids on the outer nanoparticle layer reduces the availability of surface sites for "excess CIL," resulting in their concomitant depletion from the LNP surface. A decreased superficial positive charge density would be expected to impair the efficiency of an endosomal escape process that is based on membrane fusion events and mediated by charged ionizable lipid headgroups (10).

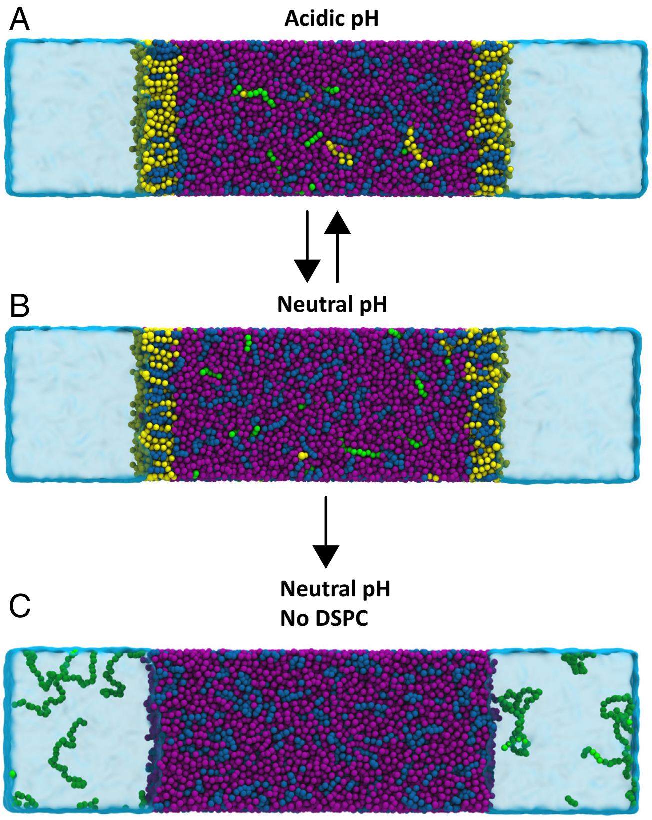

Fig. 5. The role of DSPC for LNP stability and RNA encapsulation. Variations of pH ranging from fully protonated ionizable lipid (purple) to unprotonated (*A*: acidic pH; *B*: neutral pH) did not lead to the release of RNA into the aqueous phase in the presence of DSPC (yellow). Conversely, removal of the DSPC layer (*C*) in an unprotonated environment led to RNA (green) leaving the LNP.

Once in the pH-neutral cytosol, the "complex salt" dissociates, releasing the free nucleic acid to carry out its function, such as translation into a protein for mRNA or knockdown for siRNA or ASO. Further research featuring simulations with an explicit representation of the membrane accompanied by structural experiments (60, 61) would be helpful to improve our understanding of the endosomal escape process.

RNA Concentration Affects Molecular Mobility Inside the LNP. Another factor frequently optimized for RNA-LNPs is the molar proportion of RNA to ionizable lipid, commonly referred to as the N/P ratio. Typical values range from N/P = 3 [for Onpattro (62)] to N/P = 6 [for Comirnaty (62)], and can be even higher (up to N/P = 12) for some LNPs encapsulating even larger RNA cargos, such as self-amplifying RNA (63). When dosed at the same RNA concentration, LNPs with an increased N/P ratio often lead to higher protein production in vivo; however, the increased amounts of ionizable lipid are also associated with potentially greater toxicity.

Considering this, we aimed to analyze the effect of different N/P ratios on the internal structure of LNPs and the molecular mobility of their components. RNA typically constitutes between 2% and 8% by weight of the LNP, depending on the chosen N/P ratio for the specific nanoparticle. Given the molecular length and interaction profiles of this nucleic acid, we hypothesized that RNA could decrease molecular mobility within LNPs. To better understand how RNA modulates the internal dynamics of LNPs, we conducted bulk NpT simulations of the core region of *LNP1* (approx. 7% w/w RNA at the core of the LNP) and subsequently diluted the RNA concentration by a factor of 10, resulting in *LNP3* (approx. 0.7% w/w RNA). We then computed diffusion coefficients from the mean squared displacement (64) for the components in these two formulations (Fig. 6*A*).

For every molecular species within these LNPs, a lower RNA concentration resulted in higher mobility. Decreasing the RNA concentration from 7% to 0.7% by weight increased the diffusion coefficient by an average factor of 1.5. This result leads us to postulate that RNA hinders the mobility of the other components within the nanoparticle, likely due to the nature of this nucleic acid as a long, multiply charged chain with favorable interactions with other molecules in the interior of LNPs. This finding emphasizes how the concentration of RNA (or the N/P ratio) can be used to engineer and fine-tune the material properties of LNPs. It is important to note that the modulation of molecular mobility, either by LNP composition or the structure of different ionizable lipids (65), could also play a role in the endosomal escape process and the rate at which CIL molecules can relocate toward the LNP surface to facilitate membrane fusion (*SI Appendix*, Fig. S6). In line with this, Philipp et al. recently reported a lower mobility of the ionizable lipid DLinDMA using fluorescence anisotropy, along with a delayed onset of protein production in single-cell experiments (65). This report underscores the hypothesis that ionizable lipid mobility is another key contributing factor to endosomal fusion and escape. Building on these experimental findings, the mobility calculations can serve as an additional and relevant metric to rank and characterize LNP formulations.

Encapsulation-Driven Conformational Changes. Finally, to investigate the impact of LNP encapsulation on the conformational ensemble of RNA and CIL, we determined the degree of compaction (see Fig. 6*B*) in both an aqueous environment and in the interior of LNPs. In highly diluted aqueous environments, the hydrophobic aliphatic tails of the CIL molecules fold to minimize their exposure to water and maximize intramolecular interactions. In contrast, within the interior of LNPs, the CIL can adopt extended conformations to promote interactions with other lipophilic molecules. RNA molecules in the interior of LNPs undergo an enthalpy-driven collapse, adopting more compact conformations to interact with the positively charged environment. This adaptation allows them to overcome self-repulsion from the charge–charge interactions between the negatively charged phosphate groups in the RNA backbone.

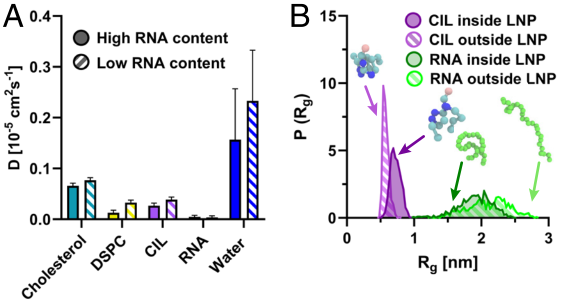

Fig. 6. Molecular mobility and structural flexibility inside LNPs. (*A*) Effect of RNA concentration on molecular mobility in LNPs by comparison of the mean squared displacement (MSD) for the molecules found inside LNPs. Weight ratios: 7% RNA (filled), and 0.7% RNA (striped); (*B*) LNP encapsulation drives compaction of RNA and expansion of CIL molecules. Comparison of the radius of gyration (Rg) distributions for RNA and CIL molecules in the interior of an LNP (continuous) and in a free aqueous environment (striped).

Conclusion

In this work, we presented a molecular dynamics approach that enables accurate simulation of full-sized LNPs (diameter > 80 nm) within a computationally feasible timeframe. This method facilitated the detailed characterization of the spatial distribution of key molecular components—RNA, ionizable lipids, cholesterol, and DSPC—within the LNP, specifically under acidic conditions that reflect a key aspect of the endosomal environment. Additionally, we illustrated how modifications in LNP formulation can significantly reshape surface nanostructure, which in turn may regulate essential processes such as endosomal escape and cellular uptake, thereby impairing overall LNP efficacy. By comparing the structural features derived from different LNP formulations with cellular assay data on LNP uptake, endosomal escape, and RNA translation, we have shed light on how these surface features could be linked to reduced activity. Furthermore, we observed the migration of ionizable lipids toward the LNP surface under low pH conditions, a phenomenon consistent with a membrane fusion-based mechanism for endosomal escape. Complementing recent studies that emphasize the role of ionizable lipid shape (66) as well as its structural transitions (65), our findings suggest that both LNP composition and internal molecular mobility may play critical roles in governing processes such as uptake and endosomal escape. These insights, along with the simulation approach, could offer a foundation to advance rational LNP design and ultimately enable the development of more efficient genomic medicines.

Methods

Direct Coexistence Simulation Details. To better understand the distribution of the different components inside LNPs, we employed the direct coexistence (DC) method (67), which is a well-validated simulation technique for investigating systems composed of multiple coexisting phases and has been widely used to determine solubilities (68, 69) and phase diagrams of crystalline solids (69–73), as well as to understand lipid organization (74) and protein phase separations (32, 75, 76). In DC simulations, the coexisting phases–LNP (lipid-rich phase) and endosomal lumen (water-rich phase)–are placed in the same simulation box. Such setup allows the characterization of the molecular organization and interactions within the LNP, as well as a detailed examination of the interface between the aqueous phase and the LNP. As mentioned in the Results section, simulating LNPs with an accurate surface-area-to-volume ratio is important for realism: Simulating reduced-size LNPs (at a fixed composition) is equivalent to increasing the surface area-to-volume ratio and could result in an unrealistic overconcentration of components on the particle's surface as opposed to locating to the core.

The area of the lipid-water interphase (Lx, Ly) was thus selected to match the surface area-to-volume ratio (SA/V) of a lipid nanoparticle of the experimentally measured radius r (SA/V = 3/r = 2/Lz), but large enough to avoid self-interactions through the periodic boundary conditions (none of which were observed throughout the simulation by checking the minimum distance between same periodic replicates). The molecular dynamics details and coarse-graining of the different components are further outlined in Supplementary Information.

The authors do not recommend direct coexistence to study LNPs of Diameter <40 nm, as this could result in unphysical interactions between the two liquid-water interphases as well as an underestimated Laplace pressure. However, such small LNPs require less computational resources and are thus ultimately better suited to be directly simulated by standard molecular dynamics, similarly to previous LNP MD simulations (11, 19, 20) (not using direct coexistence) where the entire LNP is placed in an aqueous environment. Future research is essential to elucidate how other phenomena relevant to endosomal escape can be accurately captured through advanced simulations. Key areas of interest include the adsorption of proteins onto the LNP surface, interactions and fusion between LNPs and the endosomal membrane –particularly the possible translocation of RNA through the membrane wall– and the structural mesophase changes driven by pH variation. The efficient direct coexistence approach, which has already been applied to study the free energies of membrane stalk formation (77), could be further explored and validated against direct simulations and experiments (60) to address these complex aspects of endosomal escape.

Coarse-Grained Simulations with the MARTINI3 Forcefield. The phase behavior and localization (core, surface, or solvent) of the components of LNPs in an aqueous environment are determined by water-oil transfer free energies and water-oil interfacial tensions. Thus, for the CG simulations of LNPs in this study, we employ the MARTINI3 CG forcefield (45), which is consistent with experimental measurements of water-oil transfer free energies (mean absolute error of transfer compared to the experimental data of 2 kJ mol^{-1}) (45) and interfacial tension in liquid–liquid biphasic heterogeneous mixtures (determination coefficient >0.9) (45). Further details can be found in Supplementary Information.

***LNP1* Core Simulation Details.** To gain a more detailed insight about the chemical environment around water and RNA in the interior of *LNP1*, we computed radial distribution functions for all molecular pairs involving these two components. For this purpose, we created a simulation box with a composition equal to that found in the core region of the LNP in the DC simulations. Such setup simulating a pure "core" phase of the LNP allows us to characterize the interior of the LNP, avoiding possible pollution from the interphases with water and their dependence on the surface-area-to-volume ratio. This independent treatment of the core and shell phases is especially advisable for those components that can be found preferentially at the interphase, such as DSPC or water, as well as when computing diffusion coefficients that could be affected by the presence of an interphase (perpendicular component). Taking advantage of the same simulation setup, we studied how the encapsulation of RNA or CIL in *LNP1* modulates the conformational ensemble of these molecules. We characterized how the different microenvironments, such as the interior of the LNP and the exterior aqueous endosome, would drive expansion or compaction of the RNA and the CIL.

Finally, we investigated the internal dynamics of *LNP1* and how it can be tuned by changing the concentration of RNA. We calculated the isotropic diffusion coefficient for each LNP component at different RNA weight fractions. To compute the diffusion coefficient, we measured the mean squared displacement of each molecule as a function of time and averaged between molecules of the same component, as well as among time intervals of the same length. Once the MSD was obtained, we used the Einstein relation to derive the diffusion coefficient.

LNP Preparation and Characterization. An ethanolic solution containing the four lipids in the desired molar ratio (*for LNP1:* 45:9:44:2, *for LNP2*: 75:8:15:2; respectively for LP01/DSPC/cholesterol/DMG-PEG2000) was prepared to obtain a fixed total lipid concentration of 12.5 mM. A 4:1 (w/w) mixture of eGFP mRNA and Cy5-eGFP mRNA was dissolved in RNAse-free, 50 mM citrate buffer (pH 4) at 146 μg/mL for *LNP1* and 244 μg/mL for *LNP2*. The two solutions were then combined via microfluidic mixing utilizing the NanoAssemblr Ignite system (Precision NanoSystems Inc.) at a flow rate of 12 mL/min and an organic-to-aqueous flow rate ratio of 1:3 to yield particles with a fixed amine-to-phosphate (N/P) ratio of 4.5. The resulting LNPs were dialyzed overnight against PBS (500× sample volume) using Slide-A-Lyzer G2 dialysis cassettes (20000 MWCO, Thermo Scientific) at 4 °C. RNA concentration and RNA encapsulation was measured using the Ribogreen Assay, as described previously (16). The particle size was measured using dynamic light scattering (DLS) using a Zetasizer Nano Series ZS instrument (Malvern Instruments Ltd.). LNP characterization data (size, polydispersity, and RNA encapsulation efficiency) are reported in *SI Appendix*, Table S1.

Cell Assays. HepG2 and HeLa cells were transduced with Lentivirus containing constructs for expression of a fluorescently labeled Gal9 (fluorescent tag added at the N terminus) under the control of an EF1a promoter. Stable cell pools were selected by puromycin, and functionality of the reporter was confirmed by 80 μM chloroquine treatment. Clonal selection resulted in several clones with good viability, homogeneous expression of the reporter, and strong Gal9 granule induction after treatment with 80 μM chloroquine. HepG2 and HeLa Gal9 reporter cells were maintained under standard cell culture conditions in RPMI1640 medium with 10% FCS, 1% penicillin/streptomycin, and 0.5 μg/mL puromycin (HepG2) and MEM with 10% FCS, 1% penicillin/streptomycin, and 0.5 μg/mL puromycin (HeLa). For time-lapse studies, cells were seeded at 3,500 cells (HepG2) or 2,000 cells (HeLa) in 40 μL medium per well of a 384-well, imaging-compatible microtiterplate (Perkin Elmer; Cell Carrier-384 Ultra, TC treated; #6057308) and incubated overnight in a standard incubator (37 °C, 95% humidity, 5% CO_2). On the day of treatment, LNP solutions were diluted in culture medium to 3 μg/mL (3×) and added to the cells in 20 μL, giving a final LNP concentration of 1 μg/mL. Imaging was carried out within a humidified imaging chamber on an Opera Phenix (Perkin Elmer, #HH14001000) spinning disk confocal microscope using a 20x Objective. Images were obtained every hour for 24 h using a 488 nm laser, 561 nm laser, and 640 nm laser. Image analysis and quantification was carried out with the Harmony (PerkinElmer, Waltham, MA, USA). Briefly, cells were detected in the Gal9 channel. Within the cell regions, fluorescence for Cy5 and GFP was quantified and Gal9 puncta were identified and quantified using the "Find Spot" building block in Harmony. Data were exported and analyzed and plotted in Genedata Screener (Genedata, Basel, Switzerland) or Prism (GraphPad, San Diego, CA).

Data, Materials, and Software Availability. All study data are included in the article and/or *SI Appendix*.

ACKNOWLEDGMENTS. The preliminary version of Martini 3 cholesterol model was provided by Dr. Paulo C. T. Souza and Prof. Siewert J. Marrink, who have agreed to make these parameter files accessible via the MARTINI GitHub repository (link to be found in *SI Appendix*, Supporting Information). We are grateful to Rommie Amaro for her helpful comments.

Author affiliations: [a]Drug Discovery Sciences, Bayer Pharmaceuticals, Wuppertal 42113, Germany; [b]Computational Life Science, Bayer Crop Science, Monheim am Rhein 40789, Germany; [c]Lead Discovery, Nuvisan Innovation Campus Berlin, Berlin 13353, Germany; [d]Chemical and Pharmaceutical Development, Bayer Pharmaceuticals, Turku 20210, Finland; and [e]Chemical and Pharmaceutical Development, Bayer Pharmaceuticals, Berlin 13353, Germany

1. X. Hou, T. Zaks, R. Langer, Y. Dong, Lipid nanoparticles for mRNA delivery. *Nat. Rev. Mater.* **6**, 1078–1094 (2021). 10.1038/s41578-021-00358-0.
2. K. Paunovska, D. Loughrey, J. E. Dahlman, Drug delivery systems for RNA therapeutics. *Nat. Rev. Genet.* **23**, 265–280 (2022). 10.1038/s41576-021-00439-4.
3. T. M. Allen, P. R. Cullis, Drug delivery systems: Entering the mainstream. *Science* **303**, 1818–1822 (2004). 10.1126/science.1095833.
4. F. P. Polack *et al.*, Safety and efficacy of the BNT162b2 mRNA covid-19 vaccine. *N. Engl. J. Med.* **383**, 2603–2615 (2020). 10.1056/NEJMoa2034577.
5. L. R. Baden *et al.*, Efficacy and Safety of the mRNA-1273 SARS-CoV-2 Vaccine. *N. Engl. J. Med.* **384**, 403–416 (2021). 10.1056/NEJMoa2035389.
6. P. R. Cullis, M. J. Hope, Lipid nanoparticle systems for enabling gene therapies. *Mol. Ther.* **25**, 1467–1475 (2017). 10.1016/j.ymthe.2017.03.013.
7. E. O. Blenke *et al.*, The storage and in-use stability of mRNA vaccines and therapeutics: Not a cold case. *J. Pharm. Sci.* **112**, 386–403 (2022). 10.1016/j.xphs.2022.11.001.
8. M. Yanez Arteta *et al.*, Successful reprogramming of cellular protein production through mRNA delivered by functionalized lipid nanoparticles. *Proc. Natl. Acad. Sci. U.S.A.* **115**, E3351–E3360 (2018). 10.1073/pnas.1720542115.
9. M. Cornebise *et al.*, DisCovery of a novel amino lipid that improves lipid nanoparticle performance through specific interactions with mRNA. *Adv. Funct. Mater.* **32**, 2106727 (2022). 10.1002/adfm.202106727.
10. J. A. Kulkarni, P. R. Cullis, R. van der Meel, Lipid nanoparticles enabling gene therapies: From concepts to clinical utility. *Nucleic Acid Ther.* **28**, 146–157 (2018). 10.1089/nat.2018.0721.
11. A. K. Leung *et al.*, Lipid NanopaRticles Containing siRNA synthesized by microfluidic mixing exhibit an electron-dense nanostructured core. *J. Phys. Chem. C Nanomater. Interfaces* **116**, 18440–18450 (2012). 10.1021/jp303267y.
12. A. K. Leung, Y. Y. Tam, S. Chen, I. M. Hafez, P. R. Cullis, Microfluidic mixing: a general method for encapsulating macromolecules in lipid nanoparticle systems. *J. Phys. Chem. B* **119**, 8698–8706 (2015). 10.1021/acs.jpcb.5b02891.
13. F. Sebastiani *et al.*, Apolipoprotein E binding drives structural and compositional rearrangement of mRNA-containing lipid nanoparticles. *ACS Nano* **15**, 6709–6722 (2021). 10.1021/acsnano.0c10064.
14. J. A. Kulkarni *et al.*, On the formation and morphology of lipid nanoparticles containing ionizable cationic lipids and siRNA. *ACS Nano* **12**, 4787–4795 (2018). 10.1021/acsnano.8b01516.
15. J. A. Kulkarni, D. Witzigmann, J. Leung, Y. Y. C. Tam, P. R. Cullis, On the role of helper lipids in lipid nanoparticle formulations of siRNA. *Nanoscale* **11**, 21733–21739 (2019). 10.1039/c9nr09347h.
16. M. J. Carrasco *et al.*, Ionization and structural properties of mRNA lipid nanoparticles influence expression in intramuscular and intravascular administration. *Commun Biol* **4**, 956 (2021). 10.1038/s42003-021-02441-2.

17. J. Gilbert *et al.*, Evolution of the structure of lipid nanoparticles for nucleic acid delivery: From in situ studies of formulation to colloidal stability. *J Colloid Interface Sci* **660**, 66–76 (2024). 10.1016/j.jcis.2023.12.165.
18. J. Gilbert *et al.*, On the interactions between RNA and titrateable lipid layers: Implications for RNA delivery with lipid nanoparticles. *Nanoscale* **16**, 777–794 (2024). 10.1039/d3nr03308b.
19. M. F. W. Trollmann, R. A. Bockmann, mRNA lipid nanoparticle phase transition. *Biophys. J.* **121**, 3927–3939 (2022). 10.1016/j.bpj.2022.08.037.
20. M. Paloncýová *et al.*, Atomistic insights into organization of RNA-loaded lipid nanoparticles. *J. Phys. Chem. B* **127**, 1158–1166 (2023). 10.1021/acs.jpcb.2c07671.
21. M. Cárdenas, R. A. Campbell, M. Y. Arteta, M. J. Lawrence, F. Sebastiani, Review of structural design guiding the development of lipid nanoparticles for nucleic acid delivery. *Curr. Opin. Colloid Interface Sci.* **66**, 101705 (2023). 10.1016/j.cocis.2023.101705.
22. J. Gilleron *et al.*, Identification of siRNA delivery enhancers by a chemical library screen. *Nucleic Acids Res.* **43**, 7984–8001 (2015). 10.1093/nar/gkv762.
23. S. Sabnis *et al.*, A novel amino lipid series for mRNA delivery: Improved endosomal escape and sustained pharmacology and safety in non-human primates. *Mol. Ther.* **26**, 1509–1519 (2018). 10.1016/j.ymthe.2018.03.010.
24. A. Gallud *et al.*, Time evolution of PEG-shedding and serum protein coronation determines the cell uptake kinetics and delivery of lipid nanoparticle formulated mRNA. bioRxiv [Preprint] (2021). https://www.biorxiv.org/content/10.1101/2021.08.20.457104v1 (Accessed 13 February 2024).
25. S. C. Wilson *et al.*, Real time measurement of PEG shedding from lipid nanoparticles in serum via NMR spectroscopy. *Mol. Pharm.* **12**, 386–392 (2015). 10.1021/mp500400k.
26. B. L. Mui *et al.*, Influence of polyethylene glycol lipid desorption rates on pharmacokinetics and pharmacodynamics of siRNA lipid nanoparticles. *Mol. Ther. Nucleic Acids* **2**, e139 (2013). 10.1038/mtna.2013.66.
27. N. M. Belliveau *et al.*, Microfluidic synthesis of highly potent limit-size lipid nanoparticles for in vivo delivery of siRNA. *Mol. Ther. Nucleic Acids* **1**, e37. (2012). 10.1038/mtna.2012.28.
28. A. Akinc *et al.*, Targeted delivery of RNAi therapeutics with endogenous and exogenous ligand-based mechanisms. *Mol. Ther.* **18**, 1357–1364 (2010). 10.1038/mt.2010.85.
29. P. Paramasivam *et al.*, Endosomal escape of delivered mRNA from endosomal recycling tubules visualized at the nanoscale. *J. Cell Biol.* **221**, e202110137 (2022). 10.1083/jcb.202110137.
30. S. Han *et al.*, Endosomal sorting results in a selective separation of the protein corona from nanoparticles. *Nat. Commun.* **14**, 295 (2023). 10.1038/s41467-023-35902-9.
31. A. J. C. Ladd, L. V. Woodcock, Triple-point coexistence properties of the lennard-jones system. *Chem. Phys. Lett.* **51**, 155–159 (1977). 10.1016/0009-2614(77)85375-x.
32. A. Garaizar *et al.*, Aging can transform single-component protein condensates into multiphase architectures. *Proc. Natl. Acad. Sci. U.S.A.* **119**, e2119800119 (2022). 10.1073/pnas.2119800119.
33. M. Tsanai, P. Frederix, C. F. E. Schroer, P. C. T. Souza, S. J. Marrink, Coacervate formation studied by explicit solvent coarse-grain molecular dynamics with the Martini model. *Chem. Sci.* **12**, 8521–8530 (2021). 10.1039/d1sc00374g.
34. J. D. Finn *et al.*, A single administration of CRISPR/Cas9 lipid nanoparticles achieves robust and persistent in vivo genome editing. *Cell Rep.* **22**, 2227–2235 (2018). 10.1016/j.celrep.2018.02.014.
35. J. D. Gillmore *et al.*, CRISPR-Cas9 in vivo gene editing for transthyretin amyloidosis. *N. Engl. J. Med.* **385**, 493–502 (2021). 10.1056/NEJMoa2107454.
36. M. Rubinstein, R. H. Colby, *Polymer Physics* (Oxford University Press, 2003).
37. F. Noé, A. Tkatchenko, K. R. Müller, C. Clementi, Machine Learning for Molecular Simulation. *Annu. Rev. Phys. Chem.* **71**, 361–390 (2020). 10.1146/annurev-physchem-042018-052331.
38. J. Wang *et al.*, Multi-body effects in a coarse-grained protein force field. *J. Chem. Phys.* **154**, 164113 (2021). 10.1063/5.0041022.
39. J. Wang *et al.*, Machine learning of coarse-grained molecular dynamics force fields. *ACS Cent. Sci.* **5**, 755–767 (2019). 10.1021/acscentsci.8b00913.
40. F. Grunewald, P. C. T. Souza, S. J. Marrink, The martini 3 ecosystem for coarse-grained simulations. *Biophys. J.* **122**, 419a–420a (2023). 10.1016/j.bpj.2022.11.2274.
41. G. Enkavi, M. Javanainen, W. Kulig, T. Róg, I. Vattulainen, Multiscale simulations of biological membranes: The challenge to understand biological phenomena in a living substance. *Chem. Rev.* **119**, 5607–5774 (2019). 10.1021/acs.chemrev.8b00538.
42. F. Lolicato *et al.*, The role of temperature and lipid charge on intake/uptake of cationic gold nanoparticles into lipid bilayers. *Small* **15**, e1805046 (2019). 10.1002/smll.201805046.
43. G. Rossi, L. Monticelli, S. R. Puisto, I. Vattulainen, T. Ala-Nissila, Coarse-graining polymers with the MARTINI force-field: Polystyrene as a benchmark case. *Soft. Matter.* **7**, 698–708 (2011). 10.1039/c0sm00481b.
44. S. J. Marrink, H.J. Risselada, S. Yefimov, D. P. Tieleman, A. H. de Vries, The MARTINI force field: Coarse grained model for biomolecular simulations. *J. Phys. Chem. B* **111**, 7812–7824 (2007). 10.1021/jp071097f.
45. P. C. T. Souza *et al.*, Martini 3: A general purpose force field for coarse-grained molecular dynamics. *Nat. Methods* **18**, 382–388 (2021). 10.1038/s41592-021-01098-3.
46. S. Sami, F. Grünewald, in *A Practical Guide to Recent Advances in Multiscale Modeling and Simulation of Biomolecules*. Yong Wang, Ruhong Zhou, eds. (AIP Publishing LLC, 2023).
47. F. Grünewald *et al.*, Titratable Martini model for constant pH simulations. *J. Chem. Phys.* **153**, 024118 (2020). 10.1063/5.0014258.
48. T. J. Welsh *et al.*, Surface electrostatics govern the emulsion stability of biomolecular condensates. *Nano Lett.* **22**, 612–621 (2022). 10.1021/acs.nanolett.1c03138.
49. K. An *et al.*, On the influence of nucleic acid backbone modifications on lipid nanoparticle morphology. *Langmuir* **38**, 14036–14043 (2022). 10.1021/acs.langmuir.2c01492.
50. B. R. Bzdek, J. P. Reid, J. Malila, N. L. Prisle, The surface tension of surfactant-containing, finite volume droplets. *Proc. Natl. Acad. Sci. U.S.A.* **117**, 8335–8343 (2020). 10.1073/pnas.1915660117.
51. J. R. Espinosa, C. Vega, E. Sanz, Homogeneous Ice Nucleation Rate in Water Droplets. *J. Phys. Chem. C* **122**, 22892–22896 (2018). 10.1021/acs.jpcc.8b04788.
52. M. L. Brader *et al.*, Encapsulation state of messenger RNA inside lipid nanoparticles. *Biophys. J.* **120**, 2766–2770 (2021). 10.1016/j.bpj.2021.03.012.
53. S. Patel *et al.*, Naturally-occurring cholesterol analogues in lipid nanoparticles induce polymorphic shape and enhance intracellular delivery of mRNA. *Nat. Commun.* **11**, 983 (2020). 10.1038/s41467-020-14527-2.
54. L. Zheng, S. R. Bandara, Z. Tan, C. Leal, Lipid nanoparticle topology regulates endosomal escape and delivery of RNA to the cytoplasm. *Proc. Natl. Acad. Sci. U.S.A.* **120**, e2301067120 (2023). 10.1073/pnas.2301067120.
55. M. J. Munson *et al.*, A high-throughput Galectin-9 imaging assay for quantifying nanoparticle uptake, endosomal escape and functional RNA delivery. *Commun. Biol.* **4**, 211 (2021). 10.1038/s42003-021-01728-8.
56. A. Wittrup *et al.*, Visualizing lipid-formulated siRNA release from endosomes and target gene knockdown. *Nat. Biotechnol.* **33**, 870–876 (2015). 10.1038/nbt.3298.
57. J. A. Kulkarni *et al.*, Spontaneous, solvent-free entrapment of siRNA within lipid nanoparticles. *Nanoscale* **12**, 23959–23966 (2020). 10.1039/d0nr06816k.
58. B. Leavitt *et al.,* WO2020077007A1: Compositions and systems comprising transfection-competent vesicles free of organic-solvents and detergents and methods related thereto. (2020). https://patents.google.com/patent/WO2020077007A1/de. Accessed 13 February 2024.
59. M. Maugeri *et al.*, Linkage between endosomal escape of LNP-mRNA and loading into EVs for transport to other cells. *Nat. Commun.* **10**, 4333 (2019). 10.1038/s41467-019-12275-6.
60. L. Caselli, T. Nylander, M. Malmsten, Neutron reflectometry as a powerful tool to elucidate membrane interactions of drug delivery systems. *Adv. Colloid Interface Sci.* **325**, 103120 (2024). 10.1016/j.cis.2024.103120.
61. M. Ibrahim, J. Gilbert, M. Heinz, T. Nylander, N. Schwierz, Structural insights on ionizable Dlin-MC3-DMA lipids in DOPC layers by combining accurate atomistic force fields, molecular dynamics simulations and neutron reflectivity. *Nanoscale* **15**, 11647–11656 (2023). 10.1039/d3nr00987d.
62. L. Schoenmaker *et al.*, mRNA-lipid nanoparticle COVID-19 vaccines: Structure and stability. *Int. J. Pharm.* **601**, 120586 (2021). 10.1016/j.ijpharm.2021.120586.
63. A. K. Blakney, P. F. McKay, B. I. Yus, Y. Aldon, R. J. Shattock, Inside out: Optimization of lipid nanoparticle formulations for exterior complexation and in vivo delivery of saRNA. *Gene. Ther.* **26**, 363–372 (2019). 10.1038/s41434-019-0095-2.
64. M. Javanainen *et al.*, Anomalous and normal diffusion of proteins and lipids in crowded lipid membranes. *Faraday Discuss* **161**, 397–417 discussion 419–359 (2013). 10.1039/c2fd20085f.
65. J. Philipp *et al.*, pH-dependent structural transitions in cationic ionizable lipid mesophases are critical for lipid nanoparticle function. *Proc. Natl. Acad. Sci. U.S.A.* **120**, e2310491120 (2023). 10.1073/pnas.2310491120.
66. G. Tesei *et al.*, Lipid shape and packing are key for optimal design of pH-sensitive mRNA lipid nanoparticles. *Proc. Natl. Acad. Sci. U.S.A.* **121**, e2311700120 (2024). 10.1073/pnas.2311700120.
67. A. C. L. Opitz, Molecular dynamics investigation of a free surface of liquid argon. *Phys. Lett. A* **47**, 439–440 (1974). 10.1016/0375-9601(74)90566-0.
68. J. R. Espinosa *et al.*, On the calculation of solubilities via direct coexistence simulations: Investigation of NaCl aqueous solutions and Lennard-Jones binary mixtures. *J. Chem. Phys.* **145**, 154111 (2016). 10.1063/1.4964725.
69. H. M. Manzanilla-Granados, H. Saint-Martin, R. Fuentes-Azcatl, J. Alejandre, Direct coexistence methods to determine the solubility of salts in water from numerical simulations. Test case NaCL. *J. Phys. Chem. B* **119**, 8389–8396 (2015). 10.1021/acs.jpcb.5b00740.
70. M. M. Conde, M. A. Gonzalez, J. L. Abascal, C. Vega, Determining the phase diagram of water from direct coexistence simulations: The phase diagram of the TIP4P/2005 model revisited. *J. Chem. Phys.* **139**, 154505 (2013). 10.1063/1.4824627.
71. Y. Xiong, P. S. Shabane, A. V. Onufriev, Melting points of OPC and OPC3 water models. *ACS Omega* **5**, 25087–25094 (2020). 10.1021/acsomega.0c02638.
72. E. G. Noya, C. Vega, J. P. Doye, A. A. Louis, The stability of a crystal with diamond structure for patchy particles with tetrahedral symmetry. *J. Chem. Phys.* **132**, 234511 (2010). 10.1063/1.3454907.
73. G. Avvisati, T. Dasgupta, M. Dijkstra, Fabrication of colloidal laves phases via hard tetramers and hard spheres: Bulk phase diagram and sedimentation behavior. *ACS Nano* **11**, 7702–7709 (2017). 10.1021/acsnano.7b00505.
74. M. Laner, P. H. Hunenberger, Phase-transition properties of glycerol-dipalmitate lipid bilayers investigated using molecular dynamics simulation. *J. Mol. Graph. Model* **59**, 136–147 (2015). 10.1016/j.jmgm.2015.04.012.
75. G. L. Dignon, W. Zheng, Y. C. Kim, R. B. Best, J. Mittal, Sequence determinants of protein phase behavior from a coarse-grained model. *PLoS Comput. Biol.* **14**, e1005941 (2018). 10.1371/journal.pcbi.1005941.
76. A. Garaizar, J. R. Espinosa, Salt dependent phase behavior of intrinsically disordered proteins from a coarse-grained model with explicit water and ions. *J. Chem. Phys.* **155**, 125103 (2021). 10.1063/5.0062687.
77. C. S. Poojari, K. C. Scherer, J. S. Hub, Free energies of membrane stalk formation from a lipidomics perspective. *Nat. Commun.* **12**, 6594 (2021). 10.1038/s41467-021-26924-2.